JACS
JOURNAL OF THE AMERICAN CHEMICAL SOCIETY
pubs.acs.org/JACS

Article

Unraveling the pH-Dependent Oxygen Reduction Performance on Single-Atom Catalysts: From Single- to Dual-Sabatier Optima

Di Zhang, Zhuyu Wang, Fangzhou Liu, Peiyun Yi, Linfa Peng, Yuan Chen, Li Wei,* and Hao Li*

Cite This: J. Am. Chem. Soc. 2024, 146, 3210−3219

Read Online

ACCESS | Metrics & More | Article Recommendations | Supporting Information

ABSTRACT: Metal−nitrogen−carbon (M−N−C) single-atom catalysts (SACs) have emerged as a potential substitute for the costly platinum-group catalysts in oxygen reduction reaction (ORR). However, several critical aspects of M−N−C SACs in ORR remain poorly understood, including their pH-dependent activity, selectivity for 2- or 4-electron transfer pathways, and the identification of the rate-determining steps. Herein, by analyzing >100 M−N−C structures and >2000 sets of energetics, we unveil a pH-dependent evolution in ORR activity volcanos—from a single peak in alkaline media to a double peak in acids. We found that this pH-dependent behavior in M−N−C catalysts fundamentally stems from their moderate dipole moments and polarizability for O* and HOO* adsorbates, as well as unique scaling relations among ORR adsorbates. To validate our theoretical discovery, we synthesized a series of molecular M−N−C catalysts, each characterized by well-defined atomic coordination environments. Impressively, the experiments matched our theoretical predictions on kinetic current, Tafel slope, and turnover frequency in both acidic and alkaline environments. These new insights also refine the famous *Sabatier* principle by emphasizing the need to avoid an "acid trap" while designing M−N−C catalysts for ORR or any other pH-dependent electrochemical applications.

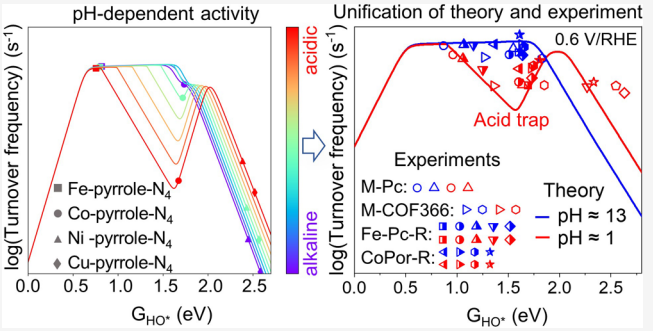

1. INTRODUCTION

Metal−nitrogen-carbon (M−N−C) single-atom catalysts (SACs) have recently garnered significant attention.[1−9] They are highly promising due to their encouraging catalytic activity for the oxygen reduction reaction (ORR) and much lower costs compared with Pt-group metal (PGM) catalysts that are typically used to overcome the sluggish ORR kinetics in fuel cells and metal−air batteries. In recent years, there has been remarkable progress in the design,[2−4] synthesis,[5] characterization,[6,7] catalytic activity, and stability evaluation[1,8,9] of M−N−C SACs. Despite these advancements, the scientific community in this field has yet to reach a unified understanding of the pH dependence, the preference of the 4-/2-electron ($4e^-$/$2e^-$) selectivity, and rate-determining steps of different M−N−C SACs, as highlighted in recent studies.[10−15]

To showcase the versatility of M−N−C catalysts, Figure 1 summarizes the reported experimental ORR activities and $4e^-$/$2e^-$ selectivity of >100 M−N−C catalysts in both acidic and alkaline media. These catalysts feature different center metals, including Mn, Fe, Co, Ni, and Cu, as well as diverse surrounding functional groups[16−22] (for more details, see Tables S1 and S2). These M−N−C catalysts include those prepared by conventional high-temperature pyrolysis of hybrid precursors constituted from carbon matrices (e.g., graphene or carbon nanotube, CNT) and metal-containing complexes.[23] We also incorporated molecular M−N−C catalysts, such as metal−organic frameworks (MOF)-derived catalysts (*e.g.*, porphyrin (POR) and phthalocyanine (Pc)) and covalent organic framework (COF)-based catalysts, which have attracted a broad range of interest in recent years due to the promoting dispersion effect for metal sites and the presence of more identical neighboring coordinated atoms around metal centers.[21,22] In light of Figure 1, three fundamental questions emerge pertaining to the pH-dependent behavior of M−N−C catalysts:

> Why do M−N−C catalysts exhibit varying pH dependence? For instance, Figure 1 indicates that certain Fe-based M−N−C catalysts appear to have less pH dependence when compared to catalysts centered around other metals. Even when the catalysts are both Fe-centered, how can we explain the better ORR performance observed on Fe-pyrrole-N_4 compared to Fe-pyridine-N_4 in acidic conditions?[1,24]
>
> How does pH affect the ORR selectivity of M−N−C catalysts? As depicted in Figure 1, what factors contribute to the generally higher selectivity for H_2O_2 observed in

Received: October 11, 2023
Revised: December 21, 2023
Accepted: December 22, 2023
Published: January 12, 2024

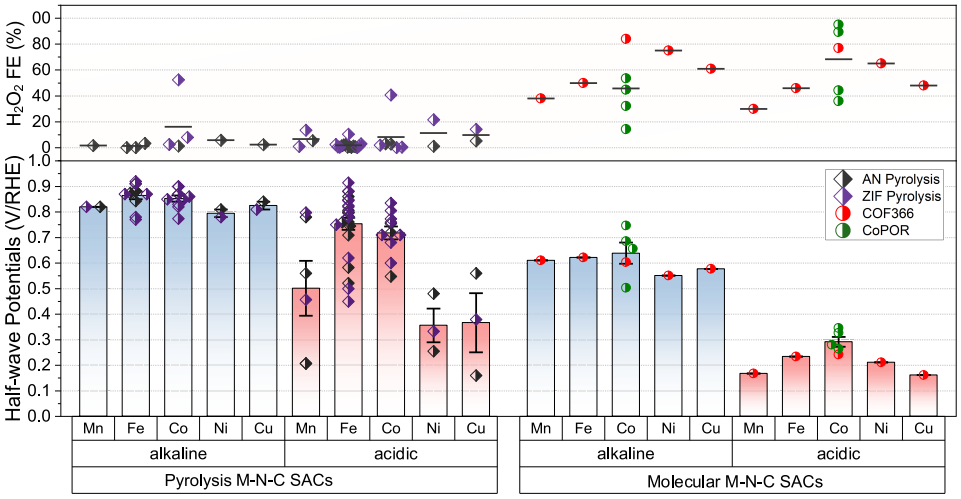

Figure 1. ORR activity analysis of >100 reported M−N−C catalysts. An overview of typical M−N−C catalysts for ORR with detailed data sources available in Tables S1 and S2. Data points were extracted from the original references based on the following conditions: the half-wave potential is the potential at which the current reaches half the value of the diffusion limiting current, and the FE is calculated at 0.6 V vs reversible hydrogen electrode (RHE). For the COF and POR-based catalysts, the potential at a current density of 0.5 mA cm^{-2} is extracted as the half-wave potential because no diffusion-limiting current can be observed. The FEs of COF and POR-based catalysts are calculated at 0.30 and 0.48 V/RHE, respectively. More details related to previous experimental data can be found in the Supporting Information.

Co-centered M−N−C catalysts,[22] and why is this selectivity further intensified in acidic conditions? Why do pyrolysis M−N−C catalysts generally exhibit a lower H_2O_2 Faradaic efficiency (FE) compared to molecular M−N−C catalysts?

What is the origin of the versatility of M−N−C SACs? To elaborate, some M−N−C catalysts exhibit insignificant pH dependence and $4e^-$-ORR selectivity comparable to PGMs in both alkaline and acidic media.[6] In the meantime, others manifest a pronounced pH sensitivity and higher FE toward H_2O_2, like many of transition metal X-ides (TMXs, X = C, N, O, etc.).[25]

To date, one of the most widely employed approaches to model electrocatalysis is the computational hydrogen electrode method[26] based on density functional theory (DFT) calculations. Although conventional thermodynamic models can capture the trends for the $2e^-$ and $4e^-$ ORR,[27] accurately predicting experimental observations, such as current density (j), half-wave potential ($E_{1/2}$), and Tafel slope, remains difficult without microkinetic modeling. Moreover, modeling the pH-dependent activity and selectivity of M−N−C catalysts presents a tougher challenge due to the absence of pH/potential-dependent free energies.[2] Recently, the origin of the high ORR activity of Fe-based M−N−C catalysts was considered to be the Fe-pyrrole-N species through DFT calculations.[28] Another theoretical study also analyzed the ORR activity of Fe−N−C catalysts by using various descriptors, such as the Fe−O bond length, the d-band center gap of spin states, and the magnetic moment of Fe-site and O_2*.[29] Regarding the remarkable H_2O_2 selectivity of Co-base M−N−C catalysts, a recent model based on constant potential explicit solvation ab initio molecular dynamics (AIMD) was developed to explain the origin of selectivity, specifically the proton adsorption to the former or later O in HOO*.[11] Despite the insights provided by these models, there is still a lack of accurate prediction of pH-dependent activity and selectivity. It is worth noting that a recent study[15] explored the electric field effects on the adsorption strengths of ORR intermediates, providing insights into why the pyrrole Fe−N−C in acidic media exhibits a higher activity than pyridinic Fe−N−C catalysts; however, the predicted pH-dependent activities differ from experimental observations regarding the onset potential under acidic and alkaline media. The urgent need for a unified model that could accurately depict the pH-dependent ORR landscape of M−N−C catalysts remains as pressing as ever.

2. METHODS

2.1. Computational Methods. For the binding energies of ORR adsorbates, DFT calculations were performed using the generalized gradient approximation method with the revised Perdew−Burke−Ernzerhof functional to describe electronic exchange and correlations.[30,31] A projector augmented-wave method was used to describe the core electrons.[32] Valence electrons were described by expanding the Kohn−Sham wave functions in a plane-wave basis set,[33] with a cutoff of at least 400 eV. We used the Quantum Espresso code[34] to calculate the electric field effects. Electric fields were applied by using a sawtooth potential that corresponds to fields ranging from −0.4 to 1.2 V/Å. At each applied field, adsorbates were allowed to relax with a force convergence threshold of 0.05 eV/Å. We used the lowest energy conformation to predict the adsorbate energy under that field. The complete computational and modeling details can be found in the Supporting Information.

2.2. Synthesis of M-COF366/CNT and MPc/CNT Catalysts. Materials and purification of as-received CNTs can be found in Supporting Information. The diameter of the CNTs is about 10−20 nm. The effect of CNT curvature on the catalytic performance can be ignored when the curvature falls within a range of 10−20 nm, and the diffusion of molecular catalysts into the inner CNT is kinetically unfavored (see Figures S1 and S2 for more details). The COF-366 decorated MWCNT catalysts were prepared by a solvothermal method. About 0.02 mmol of 5,10,15,20-(tetra-4-aminophenyl) porphine (TAPP) and 0.04 mmol of terephthaldehyde (TPD) were added to a mixture of 1 mL of absolute ethanol, 1 mL of mesitylene, and 0.1 mL of 6 M acetic acid in a Pyrex tube. Purified CNT was added at a mass ratio of 2:1 to the COF-366 precursors. The mixture was then suspended and mixed by sonication for 30 min. The tube was then subjected to three-round freeze−thaw cycles using liquid N_2, preheated to 65 °C for 4 h under Ar protection before further hydrothermally treated at 120 °C for 72 h. The solid products were then recovered by filtration and washed with EtOH and DMAC repeatedly before being dried in a vacuum. The

https://doi.org/10.1021/jacs.3c11246
J. Am. Chem. Soc. 2024, 146, 3210−3219

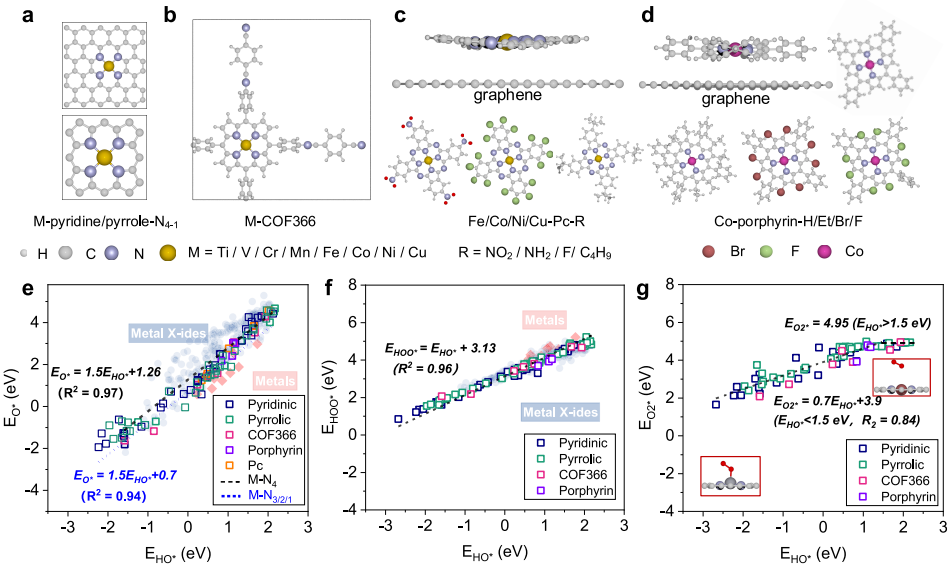

Figure 2. Linear scaling relations found in M−N−C catalysts with different atomistic environments. (a) One to four pyridine nitrogen atoms (M-pyridine-N_{4-1}) and pyrrole nitrogen atoms (M-pyrrole-N_{4-1}). (b) Conjugated porphyrin-based M-COF-366 SACs. (c) M-phthalocyanine-R. (d) Co-porphyrins-R, where R indicates different surrounding functional groups. (e) E_{HO*} vs E_{O*} scaling relation on the above M−N−C catalysts. (f) Universal scaling relation of E_{HO*} vs E_{HOO*}. (g) E_{HO*} vs E_{O_2*} scaling relation on the metal site of M−N−C catalysts. Insets show the identified chemical and physical adsorption states.

product is denoted as COF366/CNT and serves as the substrate used to prepare M-COF366/CNT catalysts. We repeated these synthesis processes to accumulate enough material for the following metalation step. Metalation of the COF366/CNT was then performed by using various metal acetate salts as metal precursors. About 45 mg of the as-prepared COF366/CNT substrate and 0.27 mmol of the metal salts were suspended in 5 mL of MeOH followed by adding 20 mL of $CHCl_3$ and 15 mL of dimethylformamide (DMF). The mixture was bath sonicated for 60 min and further stirred at 80 °C under Ar protection for 24 h. After cooling to room temperature, the solid product was recovered by filtration and washed with DI water before being dried in a vacuum. During this preparation process, the COF366 was first synthesized to coat the CNT substrate, forming a core−shell structure. Afterward, the metal was loaded to afford the M-COF366/CNT catalyst. This method could minimize the metal infiltration to inner porphyrin moieties buried inside and avoid the stacking of the metal active sites. The resulting catalysts were denoted as M-COF366/CNT, where M is Fe, Co, Ni, and Cu.

The MPc/CNT catalysts were synthesized by loading the various MPc (M = Fe, Co, Ni, and Cu) and FePc molecules with different R-groups (−R = −H, $-NH_2$, $-NO_2$, −F, and −*tert*-butyl) on the purified CNT substrate via van der Waals interactions following our reported method.[22] Briefly, about 3 mg of the MPc compounds and 20 mg of purified MWCNT were dissolved in 20 mL of DMF by ultrasonication for 30 min. Afterward, the mixture solution was stirred under an Ar environment for another 24 h before the solid products were filtered and washed with DMF (3 × 15 mL) and ethanol (10 mL) before they were dried under vacuum at 80 °C overnight to obtain the MPc/CNT catalysts.

2.3. Characterization and Electrochemical Methods. Thermogravimetric analysis (TGA) was performed on a TA Instrument TGA 5500 thermo analyzer under airflow (20 sccm). Liquid N_2 physisorption isotherms were collected on an Anton Paar Autosorb iQ analyzer. Metal residue in the purified CNT and metal loading in various catalysts were determined by inductively coupled plasma atomic emission spectroscopy (ICP-AES) on a PerkinElmer Avio 500 spectrometer. The sample was acid-digested in 6 M HNO_3 before dilution and measurement. X-ray photoelectron spectra were obtained on a Thermo Scientific K-Alpha+ spectrometer with an Al−Kα source (1486.3 eV). Samples were loaded onto a gold substrate. Survey spectra were obtained at a 1 eV step in CAE mode, with a pass energy of 200.0 eV. The high-resolution spectra were collected at a step of 0.1 eV. Transmission electron microscopy (TEM) and energy-dispersive X-ray elemental analysis were conducted on an FEI Themis-Z microscope, under either bright-field high-resolution (BF-HRTEM) or high-angle angular dark-field scanning mode (HAADF-STEM) modes. Synchrotron-illuminated X-ray absorption spectra (XAS) were collected at the XAS Beamline at the Australian Synchrotron (ANSTO). Electron beam was collected from a set of liquid nitrogen cooled Si(111) monochromators and associated Si-coated collimating and Rh-coated focusing mirrors. The beam size was about 1 × 1 mm^2. Data were collected under the transmission mode, and the energy was calibrated using corresponding metal foils. Afterward, the spectra were processed and fitted in the Demeter package using the FEFF 9.0 code.

The electrochemical performance of different catalysts was collected by using a CHI760 electrochemical workstation and a Pine MSR rotator in a three-electrode configuration at 25 °C. A rotary ring-disk electrode (RRDE, E6R1, Pine Research, with a calibrated collection efficiency N = 0.249) equipped with a glassy carbon disk (GCD, 5 mm diameter) and a Pt ring (OD = 7.50 mm, ID = 6.50 mm). The electrode was polished using Al_2O_3 powder before each measurement. A precalibrated Ag/AgCl (3 M KCl filling) reference electrode and a Hg/HgO (0.1 M KOH filling) reference electrode were used for the acidic 0.1 M $HClO_4$ and the alkaline 0.1 M KOH electrolytes, respectively. A graphite rod electrode (AFCTR3B, Pine Research) was used as the counter electrode. All reported potentials were calibrated to a reversible hydrogen electrode (V_{RHE}). The calculation method for the kinetic current densities and TOFs can be found in Supplementary Methods.

3. RESULTS AND DISCUSSION

In this study, we take the crucial first step toward understanding M−N−C SACs by DFT calculations that uncover their unique scaling relations among the adsorbate bonding strengths. 103 M−N−C catalysts with varied center metal atoms, number of coordinating N atoms, and surrounding functional groups were analyzed, including M-pyridine-N_{4-1} and M-pyrrole-N_{4-1} (Figure 2a), M-COF-366 (Figure 2b), M-phthalocyanine-R (M-Pc-R, Figure 2c), and Co-porphyrin-R (Co-POR-R, Figure 2d). Figure 2e−g presents the data collected for the respective scaling relations between the adsorption energies of O*, HOO*,

https://doi.org/10.1021/jacs.3c11246
J. Am. Chem. Soc. 2024, 146, 3210−3219

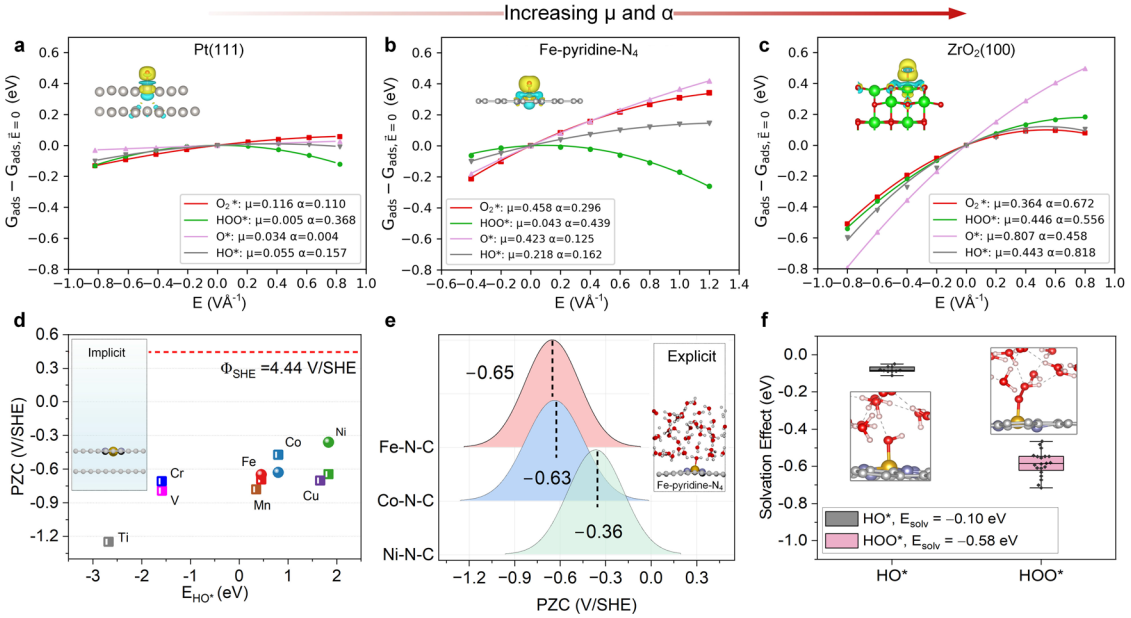

Figure 3. Field effects and other critical factors that determine the ORR activities. (a−c) Electric field effects on the adsorption free energies of ORR adsorbates with the fitted values for μ (dipole moment, eÅ) and α (polarizability, e^2 V^{-1}) for (a) Pt(111), (b) Fe-pyridine-N_4, and (c) ZrO_2(100), respectively. Insets: charge density difference induced by the adsorption of atomic oxygen. Yellow and teal colors in the isosurfaces represent electron charge gain and loss, respectively. Red, gray, and green spheres represent O, C, and Zr, respectively. The other critical factors include (d) PZCs calculated from implicit and (e) explicit models and solvation effects on the (f) binding energy changes of HO* and HOO* in the presence of explicit water molecules. The normal distributions depicted in (e) originate from over 1000 steps of the catalyst−water AIMD simulations and the box plots in (f) are derived from at least 20 distinct surface−adsorbate combinations.

and O_2* against HO*. One key finding is that the scaling relation between O* and HO* in M−N−C catalysts falls between that of transition metals (TMs) and TMXs computed based on the same level of accuracy. Interestingly, M−N−C catalysts with unsaturated nitrogen atoms (i.e., 1, 2, or 3 N atoms bonded to center metals) exhibit a lower intercept (0.7) compared to that of N_4-coordinated M−N−C catalysts (1.26) with the same slope of 1.5 (Figure 2e). A lower slope indicates stronger adsorption of ORR adsorbates on M−N−C catalysts, which is attributed to the unsaturated N coordination of the metal atom. A higher intercept indicates a weaker bonding of O* at a given HO* bonding strength, which in turn results in a larger barrier for O−O bond breaking.[25]

The second scaling relation (HO* vs HOO*) observed in Figure 2f appears to be universal, with an intercept nearly identical to those of TMs and TMXs.[25] A noteworthy discovery is that E_{O_2*} and E_{HO*} display a segmented relationship in Figure 2g: in the M−N−C catalysts with E_{HO*} values surpassing 1.5 eV, the binding energy of O_{2*} remains nearly constant at 4.95 eV due to the physical adsorption state, as depicted in the inset image in Figure 2g. The scaling relation between E_{O_2*} and E_{HO*} plays a crucial role in HOO* formation during ORR, providing an opportunity to identify the turning point from $4e^-$ to $2e^-$ ORR selectivity. All of these are borne out in the universal microkinetic model of the ORR, which is displayed in Figure 4. Because all reaction energetics have good scaling relations with E_{HO*}, a single descriptor is sufficient for microkinetic modeling.[35,36]

To develop a comprehensive model, we need to examine all relevant factors that can have a significant impact on the ORR activity of M−N−C SACs, including the potential of zero charges (PZCs), and the electric field and solvation effects. Recent studies have demonstrated that electric field effects can account for the pH dependence of weak-binding ORR catalysts.[35,37] Although it may be difficult to accurately measure the magnitude of the electric field under different electrode potentials and pH, a parallel-plate capacitor model can be used to describe the relationship between the electric field and electrode potential (vs standard hydrogen electrode, SHE).[35] The field interacts with intermediates and transition states with a substantial dipole moment (μ) and/or polarizability (α). Figure 3a−c provides an example of how ORR adsorbates on TMs,[35] M−N−C catalysts, and TMXs[25] respond to varying electric fields. In accordance with the observed scaling relations between E_{O*} and E_{HO*}, M−N−C catalysts demonstrate a moderate sensitivity (especially for the adsorbed O*) to the perturbations in electric field, as depicted by the arrow in Figure 3, when compared to this characteristic of TMX[25] and TM surfaces.[35] In Figures S2 and S3, we delve into the field response of 24 distinct M−N−C catalysts, each differing in metal centers and N coordination numbers. We found the majority of M−N−C catalysts have a μ(O*) ranging between 0.3 and 0.6 eÅ, which is notably situated between the μ(O*) values observed for TMs and TMXs. Subsequently, we will highlight how this moderate response, combined with special scaling relations, plays an essential role in the distinct pH dependence and selectivity seen in M−N−C catalysts.

The PZC serves as a pivotal parameter, dictating the electrochemical interactions at the metal−water interface. For example, it profoundly modulates the magnitude of the electric field for a given potential, subsequently dictating the configuration of the electric double layer.[38] In the present study, we evaluated the PZCs of selected M−N−C catalysts, comparing data derived from implicit models (Figure 3d) with those from AIMD simulations (Figure 3e). Our findings manifest a notable congruence between the PZCs of Fe-pyridine-N_4 and Co-pyridine-N_4 as determined by the VASPsol

https://doi.org/10.1021/jacs.3c11246
J. Am. Chem. Soc. 2024, 146, 3210−3219

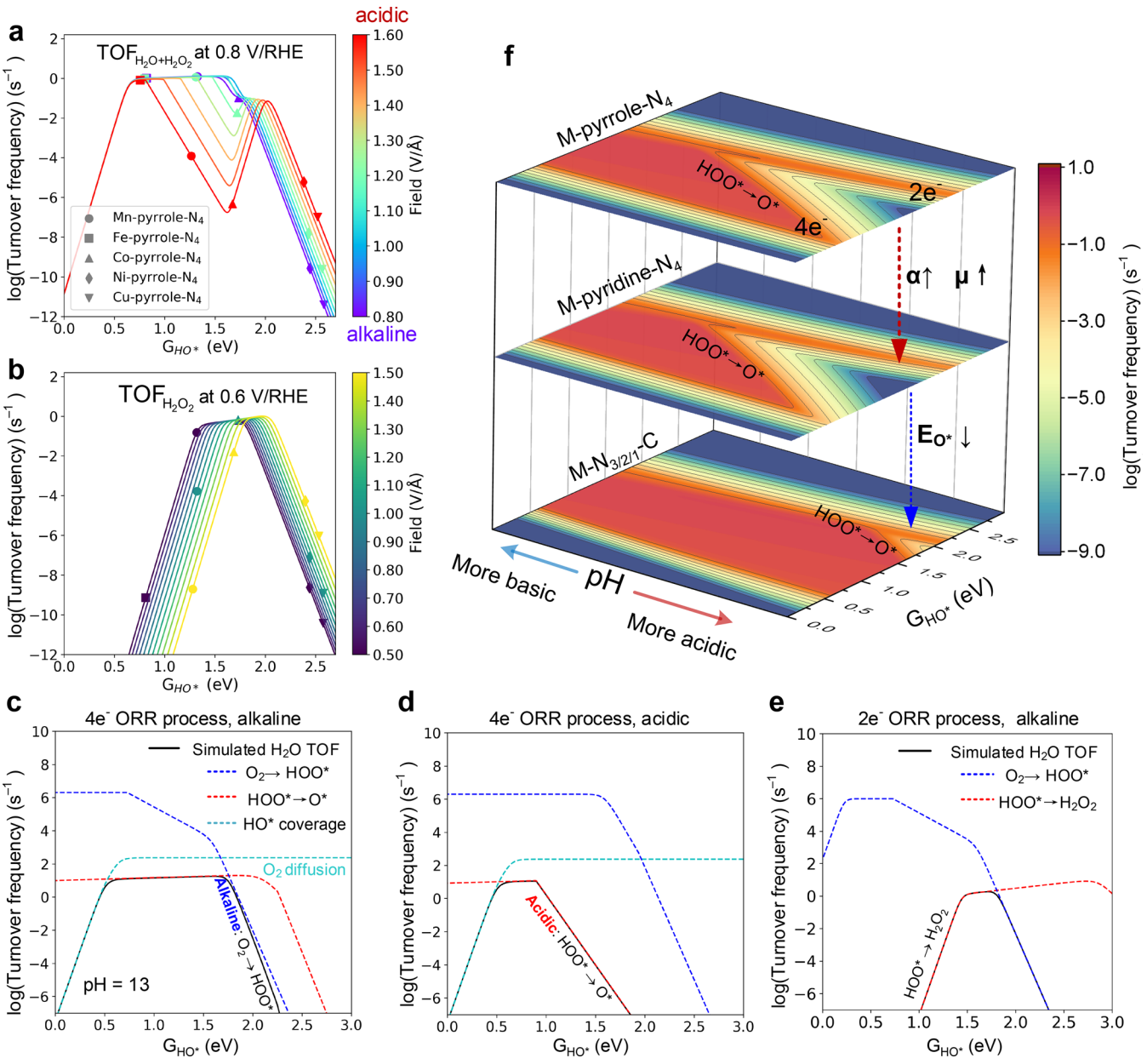

Figure 4. Microkinetic ORR volcano models of M−N−C SACs and rate-determining analyses.(a, b) Activity volcano for the (a) overall ORR TOF of M−pyrrole−N catalysts at 0.8 V/RHE, (b) 2e$^-$ ORR TOF of M−pyrrole−N catalysts at 0.6 V/RHE. Higher electric fields correspond to lower pH values. (c, d) Rate-determining analyses of the (c) 4e$^-$ ORR process in alkaline media, the (d) 4e$^-$ ORR process in acids, and the (e) 2e$^-$ ORR process in alkaline media. Dashed lines indicate the ORR activity solved by rate-determining step analysis with the rate limited by the O_2 protonation (blue), HOO* protonation and splitting (red), and HO* coverage (cyan). (f) Comparative analysis of the 2D pH-dependent volcano plots derived from differing electric field responses and unique scaling relations. The M−pyridine−N_4 exhibits a greater sensitivity to electric fields compared to M−pyrrole−N_3, which results in a pronounced "acid trap" (red dashed arrow). Additionally, the M-$N_{3/2/1}$ catalysts have a distinctively lower intercept (E_{O*} = 1.5E_{HO*} + 0.7) than M-N_4 catalysts (E_{O*} = 1.5E_{HO*} + 1.26), contributing to diminished 2e$^-$ selectivity.

implicit model and those extrapolated from AIMD.[39] Contrarily, the PZCs of Ni-pyridine-N_4, when determined by both methods, exhibit a deviation of 0.3 V/SHE. Throughout AIMD simulations, the Ni-pyridine-N_4 surface demonstrates a minimal interaction with water molecules, whereas the Fe/Co-pyridine-N_4 surfaces potentially adsorb a water molecule onto the central metal atom (refer to Supplementary Movie 1, Movie 2, and Movie 3 for a comprehensive view). This suggests that the implicit model might possess inherent limitations in accurately describing PZCs when water molecules establish distinct interactions with the material surfaces. According to our computational results, the PZCs of M−N−C catalysts predominantly lie within a range of −0.3 to −0.6 V/SHE. This range also contrasts with the PZCs of TM surfaces, which are conventionally observed to be positive.[35] In pursuit of a unified model for this research, we employed an average value of the PZCs deduced from the AIMD simulations to derive microkinetic activity models.

Solvation effects are also important for electrochemical reactions that take place at the electrode−electrolyte interface.[40] In this work, we analyze the influence of explicit solvation on the stability of adsorbed intermediates during the ORR on M−N−C catalysts. Previous research has reported explicit solvent stabilization of HO* on Pt(111), with reported values of 0.1−

https://doi.org/10.1021/jacs.3c11246
J. Am. Chem. Soc. 2024, 146, 3210−3219

0.3 eV depending on coverage.[26] Tripkovic et al.[41] found HOO* to be stabilized by 0.5 eV using a half-dissociated water layer network on Pt(111). Liu et al.[42] found that O* and O_2* experience minimal stabilizations, while HO* and HOO* are stabilized by approximately 0.6 and 0.7 eV, respectively. Notably, although the solvation effects of these oxygen species have been extensively examined on PGMs, the extent to which adsorbates on M−N−C catalysts are affected by solvation remains a less explored area. Herein, we examine the solvation effects on the Fe−pyridine−N catalyst surface through AIMD simulations using explicit water molecules. For each adsorbate, we uniformly sampled 20 substrate−adsorbate combinations from a pool of >1000 steps generated by AIMD simulations (other details are shown in Supplementary Methods). As a result, we apply mean values of −0.1 and −0.58 eV to adjust the adsorption energies of HO* and HOO*, respectively, to model solvation effects.

Based on our comprehensive analysis that combined all pertinent factors mentioned above, we have formulated pH-dependent microkinetic models for M−N−C catalysts. Distinct from the ORR volcano plots previously observed for TMs or TMXs,[25,35,36] the ORR volcano of M−N−C SACs exhibits a unique dynamic evolution from a single peak (i.e., the *Sabatier* optimum) in alkaline conditions to a double peak in acidic environments. In Figure 4a, the two peaks represent the $4e^-/2e^-$ activity peaks at 0.8 V/RHE, respectively. An "acid trap" creates this division between them, as seen in the same figure. For further clarification, the $2e^-$ volcanos at 0.6 V/RHE are also presented in Figure 4b. On the pH-dependent volcano plots, several representative M−N−C catalysts are indicated, and their pH-dependent behaviors remarkably align with previous experimental observations summarized in Figure 1, except for Cu/Ni-based catalysts in alkaline media, likely due to the existence of active sites other than the metal atop-site for these weaker bonding catalysts. For instance, the ORR activity of pyrrole-N-type Fe−N−C has been experimentally confirmed to be superior in both acidic and alkaline solutions.[1] Our model also reflects this, with the calculated Fe-pyrrole-N_4 data point (represented as squares in Figure 4a) meeting both the acidic and the alkaline peaks concurrently. Figure S5h details the ORR activity of pyridine-N-type Fe−N−C, revealing that Fe-pyridine-N_4 exhibits reduced activity in acidic conditions compared to Fe-pyrrole-N_4. Furthermore, the higher $2e^-$ selectivity of Co-centered M−N−C catalysts, previously substantiated in experiments and shown in Figure 1, is also mirrored in our model, as shown in Figure 4b (upper triangles). These findings offer preliminary evidence of the model's reliability and its potential in predicting the performance of newly designed M−N−C catalysts.

For a deeper understanding, Figure 4c−e depicts the reaction rate analysis of elementary ORR steps on M−N−C catalysts for the $4e^-$-alkaline, $4e^-$-acidic, and $2e^-$ processes. The transition from a single peak to a double peak in these volcanoes arises from the distinct rate-determining steps (RDS). When the adsorption strength of hydroxyl is strong, HO* removal is typically regarded as the RDS, consistent with the volcanoes observed on TMs and TMXs.[25] As G_{HO*} shifts to more positive values, M−N−C catalysts exhibit a unique scaling compared with TMXs or TMs. Specifically, for M−N−C, the scaling relation is $E_{O*} = 1.5E_{HO*} + 1.26$. In contrast, TMXs and TMs follow $E_{O*} = 2.0E_{HO*} + 0.87$[25] and $E_{O*} = 2.0E_{HO*} + 0.20$,[36] respectively. This suggests that M−N−C catalysts have stronger O* adsorption than TMXs, yet weaker than TMs when the descriptor E_{HO*} lies between 0.8−2.0 eV. Consequently, M−N−C catalysts are generally more efficient at facilitating O−O bond breaking compared to TMXs but may produce more H_2O_2 than TMs. Further comparisons can be found in Figure S5. Figure 4c illustrates that in alkaline solutions, the right leg of the M−N−C volcanoes is constrained by O_2 protonation. Conversely, in acidic solutions, the increased field response of the O* and HOO* on M−N−C catalysts, combined with their lower PZCs, leads to more positive G_{O*} and more negative G_{HOO*}. As a result, the breaking of the O−O bond in HOO* emerges as the primary controlling factor (Figure 4d). In the $2e^-$ ORR process (as depicted in Figure 4e), the RDS for H_2O_2 production is predominantly the $HOO^* + H^+ + e^- \rightarrow H_2O_2$ step, which competes with the $HOO^* + H^+ + e^- \rightarrow O^* + H_2O$ step. Essentially, the $4e^-/2e^-$ selectivity is determined by whether HOO* prefers to accept a proton−electron pair or to break the O−O bond. This observation aligns with findings from a recent AIMD study.[11] Therefore, assuming that the free energy of dissolved H_2O_2 remains constant with electrode potential, the pH dependence of the $4e^-/2e^-$ selectivity can be mainly attributed to the field effects on HOO* and O*. Specifically, we find that the HOO* adsorbates always display the largest polarizability among other ORR adsorbates, resulting in a significant stabilization effect in acidic solutions. This is consistent with experimental results that M−N−C catalysts generally exhibit a greater $2e^-$ ORR selectivity in acid compared to that in alkaline (Figure 1).[22] These discoveries reveal the fundamental reasons for the pH-dependent performance and selectivity of M−N−C catalysts.

With these enhanced understandings, we will demonstrate the strength of our model in elucidating the unique properties of M−N−C catalysts. Figure 4f illustrates the variations in the ORR turnover frequency (TOF) as a function of pH conditions (delineated by the blue and red solid arrows) and the descriptor G_{HO*}. These variations can be attributed to the interplay of distinct electric field responses and unique scaling relations. For instance, the dashed red arrow in Figure 4f indicates that pyridine−N catalysts exhibit lower ORR activities in acidic environments due to their relatively larger dipole moments (as detailed in Table S5). This nuanced observation is the essential reason for the superiority of Fe−pyrrole−N over Fe−pyridine−N in acidic ORR experiments.[1,28] Furthermore, the intrinsic scaling relations of M−N−C catalysts critically influence the contour of the 2D pH-dependent volcano plot. As shown in Figure 2e, an intercept of scaling relations for unsaturated N-coordinated M−N−C catalysts ($M\text{-}N_{3/2/1}$) that is approximately 0.5 eV lower suggests that HOO* is more inclined to undergo O−O bond dissociation than to accept a proton−electron pair and then generate H_2O_2. This behavior results in reduced H_2O_2 selectivity, as indicated by the blue dashed arrow in Figure 4f. Our model thus provides a clear explanation for the observed lower H_2O_2 FE in the M−N−C catalysts using standard pyrolysis methods (Figure 1, upper left).

The pH-dependent model presented in this study offers a comprehensive understanding of the behavior of M−N−C catalysts. However, when considering their potential for predicting and designing novel ORR catalysts, more rigorous validations are essential. To obtain the intrinsic activity of identically coordinated metal atoms within M−N−C catalysts, we experimentally synthesized 13 heterogeneous molecular M−N−C catalysts with precise structures. These molecular catalysts are further categorized into three groups based on central metals and adjoining functional groups: M-COF366, M-Pc, and Fe−

https://doi.org/10.1021/jacs.3c11246
J. Am. Chem. Soc. 2024, 146, 3210−3219

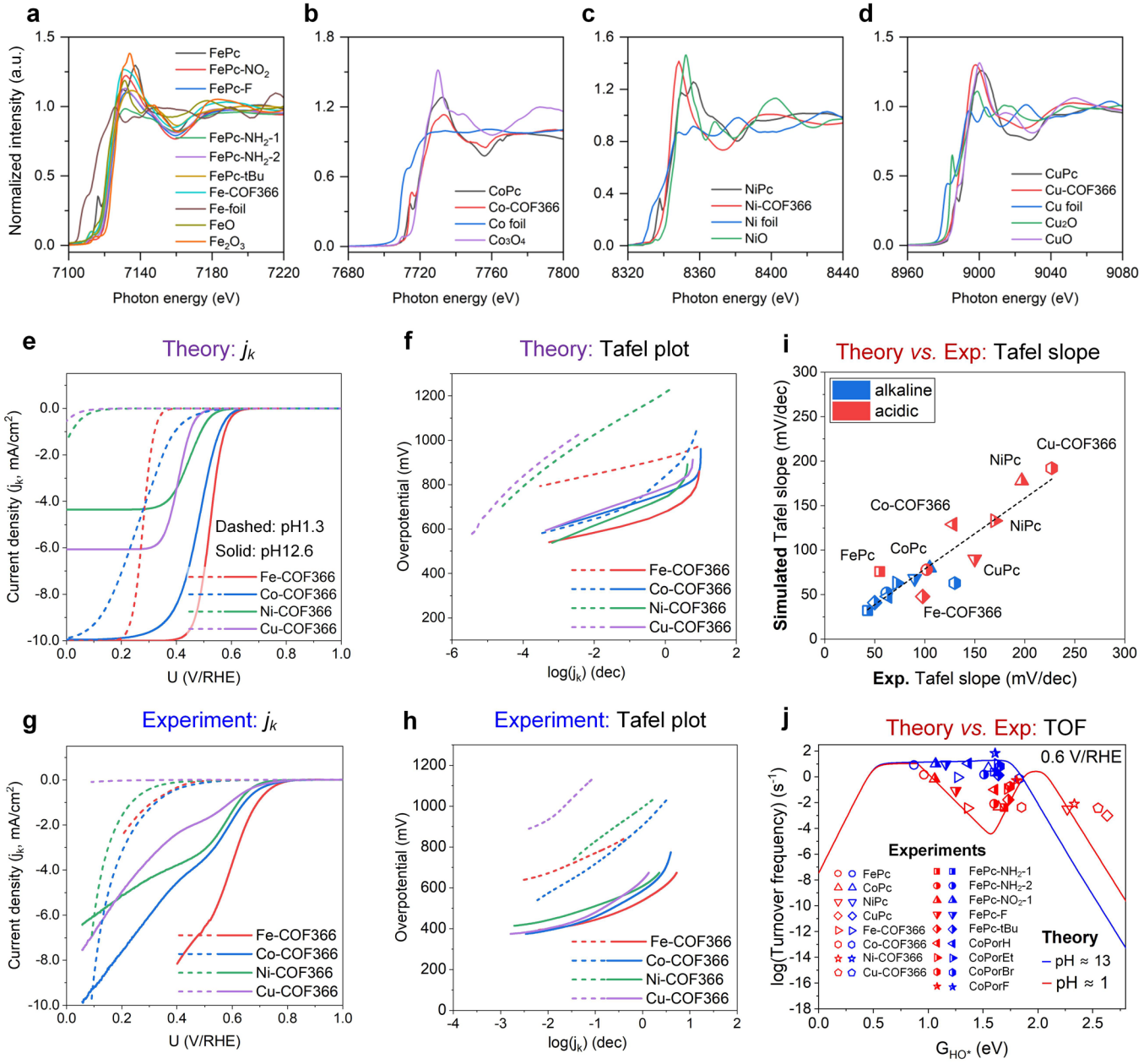

Figure 5. Experimental characterization, performance tests, and theoretical predictions.(a−e) Metal K-edge X-ray absorption near-edge structure (XANES) of the MPc/CNT, FePc/CNT-R, and M-COF366/CNT catalysts and their reference samples. (a) Fe-based, (b) Co-based, (c) Ni-based, and (d) Cu-based. Corresponding fitted k^3-weighted FT-EXAFS spectra are available in Figure S12. (e) Simulated j_K at pH 1.3 (dashed line) and 12.6 (solid line) and (f) simulated Tafel plot for the typical M-COF366 catalysts. (g) Experimental j_K at pH 1.3 (dashed line) and 12.6 (solid line) and (h) experimental Tafel plots for the typical M-COF366 catalysts. (i) Correlation plot of the experimental and simulated Tafel plots. (j) TOF of the molecular M−N−C catalysts obtained from experimental measurements and theoretical predictions.

Pc−R (for structural details, see Figures 2 and S6−S12). We performed comprehensive characterizations on these catalysts (details in Supporting Information). The synchrotron illuminated metal K-edge X-ray absorption near-edge structure (XANES) spectra, as shown in Figure 5a−d, and their extended X-ray absorption fine structure (EXAFS, Figure S12 and Table S6) fitting results confirmed that the metals are solely distributed in the M-N_4 configuration. Besides, we also assessed the ORR activity of the pristine CNT and COF366/CNT substrates (see Figure S13 for structural details) collected in acidic and alkaline electrolytes to assess the contribution of metal-free sites, e.g., doped carbon or nitrogen groups. As depicted in Figure S14, both substrates exhibit appreciable ORR current in alkaline electrolyte but remain much inferior to any of the SACs assessed here, ruling out the contribution of the substrates. Besides, to offer a reasonable comparison between our experimental and theoretical results, we calculated the site-specific TOF from the O_2-diffusion corrected kinetic current density (j_K) obtained from the Koutecky−Levich equation, and they were used as the primary performance benchmarks. Additionally, we also integrated prior experimental findings from other studies.[21,22]

Excitingly, when the simulated j_K in Figure 5e is compared with the experimental j_K in Figure 5g, the predicted onset potentials and curve shapes under different pH conditions are perfectly consistent with experimental results for the M-COF366 series. Similar results for the M-Pc series can be

https://doi.org/10.1021/jacs.3c11246
J. Am. Chem. Soc. 2024, 146, 3210−3219

found in Figure S15. Additionally, Tafel slopes for both alkaline (solid lines) and acidic conditions (dashed lines) for the simulated and experimentally observed j_K currents are illustrated in Figure 5f,h, respectively. After further analysis of these Tafel plots, a correlation plot between the predicted and experimental Tafel slopes is given in Figure 5i, demonstrating the notable consistency between the model predictions and the experimental data. Certain catalysts manifest deviations of approximately 30 mV dec^{-1}. These discrepancies may stem from the intrinsic prefactors and PZCs associated with the real reactions and catalyst structures. Nevertheless, our model provides an accurate fundamental trend in the rate-limiting step alterations, attributing to the integration of transition states and field effects. Most importantly, the "acid trap" area identified by our theoretical model is further validated by experimental TOF results (detailed TOF plots can be found in Figure S16). As discussed previously, the ORR activities of M−N−C catalysts in an acidic environment are initially constrained by the HOO*-to-O* transition and subsequently by the HOO*-to-H_2O_2 transition. Interestingly, experimental data in Figure 5j reveals that the acidic ORR TOF of molecular M−N−C catalysts first undergoes a noticeable decline followed by an increase attributed to H_2O_2 production. A comparison between simulated and experimental 2e-TOF for the M−N−C catalysts can be found in Figure S17. Therefore, during the design of ORR catalysts for fuel cell or H_2O_2 production, our model advises caution against venturing into the pH-dependent acidic trap region, where the ORR activities for both $2e^-$ and $4e^-$ are low.

4. CONCLUSIONS

This research offers deep insights into the pH-dependent ORR behavior of M−N−C catalysts and introduces a comprehensive model that can be potentially applied to other electrocatalytic processes. Returning to the initial key questions raised by Figure 1, this study presents a unified model that comprehensively addresses each of them and reveals that the pH dependence of M−N−C catalysts essentially originates from their moderate dipole moments and polarizability for the adsorbates O* and HOO* as well as their unique scaling relations among ORR adsorbates. By considering all relevant factors related to the $2e^-$/$4e^-$ ORR pathways, such as thermodynamics, kinetics, PZCs, and environmental corrections, we carefully identified the different rate-determining steps in acidic and alkaline media. Based on these new insights, the key to improving the acidic activity of M−N−C catalysts is to lower the energetics of O−O bond breaking in the HOO* → O* step. Promising approaches might include exploring M−N−C catalyst structures or active sites that exhibit optimal HO* adsorption energy and reduced O* dipole moments or utilizing an external electromagnetic field to stabilize O* adsorption.

To tune the selectivity of M−N−C catalysts, our analysis suggests that the primary focus should be a comparison of the energetics of the O−O bond breaking in HOO* and the protonation barrier from *OOH to H_2O_2. This fundamental principle could enable the rapid evaluation of the $2e^-/4e^-$ preference of a M−N−C catalyst across various pH conditions. For more precise estimations, it is essential to consider the potential-dependent free energies and accurate PZCs. The classic *Sabatier* principle tells us that for good catalysis, the binding strengths of adsorbates should not be too tight nor too loose. Adding to this, our study warns against designing M−N−C catalysts where the adsorbates are in the so-called "acid trap". In this zone, both the $2e^-$ and $4e^-$ ORR are less efficient. With these findings, scientists have a clearer roadmap to tailor the behavior of M−N−C catalysts. This knowledge can fine-tune their activity based on pH, paving the way for breakthroughs in ORR catalysis and any other electrochemical reactions influenced by pH.

■ ASSOCIATED CONTENT

Data Availability Statement

The data that support the findings of this study are included in the published article and its Supporting Information. All other data are available from the authors upon reasonable request. In addition to being available upon request, an online database on M−N−C catalysts in ORR can be accessed via the URL in the README.md file at: https://github.com/M-N-Cs/pH-dependency/.

Supporting Information

The Supporting Information is available free of charge at https://pubs.acs.org/doi/10.1021/jacs.3c11246.

pH-Dependent summary of M−N−C catalysts, detailed computational and experimental computational methods, Intrinsic dipole moment (μ) and polarizability (α) of M-pyridine/pyrrole-N catalysts, pH-dependent volcano models for typical catalysts, experimental benchmark for the 2e-ORR kinetic volcano plot, kinetic current densities and Tafel slope fitting for MePc/CNT, characterization and electrochemical performance of the CNT and COF366/CNT substrate, Microstructural characterization results, metal loading determined by ICP-AES, EXAFS fitting results, and experimental turnover frequency (PDF)

AIMD simulation of explicit water molecule modeling on Fe-pyridine-N_4 (MOV)

AIMD simulation of explicit water molecule modeling on Co-pyridine-N_4 (MOV)

AIMD simulation of explicit water molecule modeling on Ni-pyridine-N_4 (MOV)

■ AUTHOR INFORMATION

Corresponding Authors

Li Wei − *School of Chemical and Biomolecular Engineering, The University of Sydney, Sydney, New South Wales 2006, Australia;* orcid.org/0000-0001-8771-2921; Email: l.wei@sydney.edu.au

Hao Li − *Advanced Institute for Materials Research (WPI-AIMR), Tohoku University, Sendai 980-8577, Japan;* orcid.org/0000-0002-7577-1366; Email: li.hao.b8@tohoku.ac.jp

Authors

Di Zhang − *Advanced Institute for Materials Research (WPI-AIMR), Tohoku University, Sendai 980-8577, Japan; State Key Laboratory of Mechanical System and Vibration, Shanghai Jiao Tong University, Shanghai 200240, China;* orcid.org/0000-0001-6347-9344

Zhuyu Wang − *School of Chemical and Biomolecular Engineering, The University of Sydney, Sydney, New South Wales 2006, Australia*

Fangzhou Liu − *School of Chemical and Biomolecular Engineering, The University of Sydney, Sydney, New South Wales 2006, Australia;* orcid.org/0000-0001-9204-5481

Peiyun Yi − *State Key Laboratory of Mechanical System and Vibration, Shanghai Jiao Tong University, Shanghai 200240, China*

Linfa Peng − *State Key Laboratory of Mechanical System and Vibration, Shanghai Jiao Tong University, Shanghai 200240, China*

Yuan Chen − *School of Chemical and Biomolecular Engineering, The University of Sydney, Sydney, New South Wales 2006, Australia;* orcid.org/0000-0001-9059-3839

Complete contact information is available at: https://pubs.acs.org/10.1021/jacs.3c11246

Notes

The authors declare no competing financial interest.

■ ACKNOWLEDGMENTS

This research was supported by JSPS KAKENHI (No. JP23K13703), the Iwatani Naoji Foundation, and the Hirose Foundation. We acknowledge the Center for Computational Materials Science, Institute for Materials Research, Tohoku University for the use of MASAMUNE-IMR (No. 202212-SCKXX-0204), and the Institute for Solid State Physics (ISSP) at the University of Tokyo for the use of their supercomputers. H.L. and L.W. acknowledge the financial and technical support provided by the University of Sydney under the International SDG Collaboration Program, the Australian Centre for Microscopy & Microanalysis (ACMM), and the Sydney Informatics Hub (SIH) and also acknowledge the computational resources provided by the National Computational Infrastructure (NCI). L.W. acknowledges the funding support provided by the Australian Research Council Future Fellowship (Grant No. ARC-FT210100218). D.Z. acknowledges the support of the China National Postdoctoral Program for Innovative Talents from the China Postdoctoral Science Foundation (No. BX2021178) and National Natural Science Foundation of China (No. 22309109). D.Z. gratefully acknowledges the support provided by the Shanghai Jiao Tong University Outstanding Doctoral Student Development Fund and Siyuan-1 cluster supported by the Center for High Performance Computing at Shanghai Jiao Tong University.

■ REFERENCES

(1) Liu, S.; Li, C.; Zachman, M. J.; Zeng, Y.; Yu, H.; Li, B.; Wang, M.; Braaten, J.; Liu, J.; Meyer, H. M.; et al. Atomically dispersed iron sites with a nitrogen−carbon coating as highly active and durable oxygen reduction catalysts for fuel cells. *Nature Energy* **2022**, *7* (7), 652−663.

(2) Li, B.; Holby, E. F.; Wang, G. Mechanistic insights into metal, nitrogen doped carbon catalysts for oxygen reduction: progress in computational modeling. *Journal of Materials Chemistry A* **2022**, *10* (45), 23959−23972.

(3) Xu, H.; Cheng, D.; Cao, D.; Zeng, X. C. A universal principle for a rational design of single-atom electrocatalysts. *Nature Catalysis* **2018**, *1* (5), 339−348.

(4) Zhao, X.; Levell, Z. H.; Yu, S.; Liu, Y. Atomistic Understanding of Two-dimensional Electrocatalysts from First Principles. *Chem. Rev.* **2022**, *122* (12), 10675−10709.

(5) He, Y.; Liu, S.; Priest, C.; Shi, Q.; Wu, G. Atomically dispersed metal−nitrogen−carbon catalysts for fuel cells: advances in catalyst design, electrode performance, and durability improvement. *Chem. Soc. Rev.* **2020**, *49* (11), 3484−3524.

(6) Chung, H. T.; Cullen, D. A.; Higgins, D.; Sneed, B. T.; Holby, E. F.; More, K. L.; Zelenay, P. Direct atomic-level insight into the active sites of a high-performance PGM-free ORR catalyst. *Science* **2017**, *357* (6350), 479−484.

(7) Snitkoff-Sol, R. Z.; Friedman, A.; Honig, H. C.; Yurko, Y.; Kozhushner, A.; Zachman, M. J.; Zelenay, P.; Bond, A. M.; Elbaz, L. Quantifying the electrochemical active site density of precious metal-free catalysts in situ in fuel cells. *Nature Catalysis* **2022**, *5* (2), 163−170.

(8) Shao, Y.; Dodelet, J.-P.; Wu, G.; Zelenay, P. PGM-Free Cathode Catalysts for PEM Fuel Cells: A Mini-Review on Stability Challenges. *Adv. Mater.* **2019**, *31* (31), 1807615.

(9) Martinez, U.; Komini Babu, S.; Holby, E. F.; Chung, H. T.; Yin, X.; Zelenay, P. Progress in the Development of Fe-Based PGM-Free Electrocatalysts for the Oxygen Reduction Reaction. *Adv. Mater.* **2019**, *31* (31), 1806545.

(10) Zhao, C.-X.; Li, B.-Q.; Liu, J.-N.; Zhang, Q. Intrinsic Electrocatalytic Activity Regulation of M−N−C Single-Atom Catalysts for the Oxygen Reduction Reaction. *Angew. Chem., Int. Ed.* **2021**, *60* (9), 4448−4463.

(11) Zhao, X.; Liu, Y. Origin of Selective Production of Hydrogen Peroxide by Electrochemical Oxygen Reduction. *J. Am. Chem. Soc.* **2021**, *143* (25), 9423−9428.

(12) Liu, K.; Qiao, Z.; Hwang, S.; Liu, Z.; Zhang, H.; Su, D.; Xu, H.; Wu, G.; Wang, G. Mn- and N- doped carbon as promising catalysts for oxygen reduction reaction: Theoretical prediction and experimental validation. *Applied Catalysis B: Environmental* **2019**, *243*, 195−203.

(13) Wang, Y.; Tang, Y.-J.; Zhou, K. Self-Adjusting Activity Induced by Intrinsic Reaction Intermediate in Fe−N−C Single-Atom Catalysts. *J. Am. Chem. Soc.* **2019**, *141* (36), 14115−14119.

(14) Stevens, M. B.; Anand, M.; Kreider, M. E.; Price, E. K.; Zeledón, J. Z.; Wang, L.; Peng, J.; Li, H.; Gregoire, J. M.; Hummelshøj, J.; et al. New challenges in oxygen reduction catalysis: a consortium retrospective to inform future research. *Energy Environ. Sci.* **2022**, *15* (9), 3775−3794.

(15) Hu, X.; Chen, S.; Chen, L.; Tian, Y.; Yao, S.; Lu, Z.; Zhang, X.; Zhou, Z. What is the Real Origin of the Activity of Fe−N−C Electrocatalysts in the O2 Reduction Reaction? Critical Roles of Coordinating Pyrrolic N and Axially Adsorbing Species. *J. Am. Chem. Soc.* **2022**, *144* (39), 18144−18152.

(16) Rojas-Carbonell, S.; Artyushkova, K.; Serov, A.; Santoro, C.; Matanovic, I.; Atanassov, P. Effect of pH on the Activity of Platinum Group Metal-Free Catalysts in Oxygen Reduction Reaction. *ACS Catal.* **2018**, *8* (4), 3041−3053.

(17) Ge, X.; Sumboja, A.; Wuu, D.; An, T.; Li, B.; Goh, T.; Hor, T.; Zong, Y.; Liu, Z. Oxygen Reduction in Alkaline Media: From Mechanisms to Recent Advances of Catalysts. *ACS Catal.* **2015**, *5*, 4643−4667.

(18) Wan, K.; Yu, Z.-P.; Li, X.-H.; Liu, M.-Y.; Yang, G.; Piao, J.-H.; Liang, Z.-X. pH Effect on Electrochemistry of Nitrogen-Doped Carbon Catalyst for Oxygen Reduction Reaction. *ACS Catal.* **2015**, *5* (7), 4325−4332.

(19) Zhong, W.; Wang, Z.; Han, S.; Deng, L.; Yu, J.; Lin, Y.; Long, X.; Gu, M.; Yang, S. Identifying the Active Sites of a Single Atom Catalyst with pH-Universal Oxygen Reduction Reaction Activity. *Cell Reports Physical Science* **2020**, *1* (7), No. 100115.

(20) Peng, H.; Liu, F.; Liu, X.; Liao, S.; You, C.; Tian, X.; Nan, H.; Luo, F.; Song, H.; Fu, Z.; et al. Effect of Transition Metals on the Structure and Performance of the Doped Carbon Catalysts Derived From Polyaniline and Melamine for ORR Application. *ACS Catal.* **2014**, *4* (10), 3797−3805.

(21) Liu, C.; Li, H.; Liu, F.; Chen, J.; Yu, Z.; Yuan, Z.; Wang, C.; Zheng, H.; Henkelman, G.; Wei, L.; et al. Intrinsic Activity of Metal Centers in Metal−Nitrogen−Carbon Single-Atom Catalysts for Hydrogen Peroxide Synthesis. *J. Am. Chem. Soc.* **2020**, *142* (52), 21861−21871.

(22) Liu, C.; Yu, Z.; She, F.; Chen, J.; Liu, F.; Qu, J.; Cairney, J. M.; Wu, C.; Liu, K.; Yang, W.; et al. Heterogeneous molecular Co−N−C catalysts for efficient electrochemical H2O2 synthesis. *Energy Environ. Sci.* **2023**, *16* (2), 446−459.

(23) Peng, Y.; Lu, B.; Chen, S. Carbon-Supported Single Atom Catalysts for Electrochemical Energy Conversion and Storage. *Adv. Mater.* **2018**, *30* (48), 1801995.

(24) Tian, X.; Zhao, X.; Su, Y.-Q.; Wang, L.; Wang, H.; Dang, D.; Chi, B.; Liu, H.; Hensen, E. J. M.; Lou, X. W.; et al. Engineering bunched Pt-Ni alloy nanocages for efficient oxygen reduction in practical fuel cells. *Science* **2019**, *366* (6467), 850−856.
(25) Li, H.; Kelly, S.; Guevarra, D.; Wang, Z.; Wang, Y.; Haber, J. A.; Anand, M.; Gunasooriya, G. T. K. K.; Abraham, C. S.; Vijay, S.; et al. Analysis of the limitations in the oxygen reduction activity of transition metal oxide surfaces. *Nature Catalysis* **2021**, *4* (6), 463−468.
(26) Nørskov, J. K.; Rossmeisl, J.; Logadottir, A.; Lindqvist, L.; Kitchin, J. R.; Bligaard, T.; Jónsson, H. Origin of the Overpotential for Oxygen Reduction at a Fuel-Cell Cathode. *J. Phys. Chem. B* **2004**, *108* (46), 17886−17892.
(27) Viswanathan, V.; Hansen, H. A.; Rossmeisl, J.; Nørskov, J. K. Unifying the 2e− and 4e− Reduction of Oxygen on Metal Surfaces. *J. Phys. Chem. Lett.* **2012**, *3* (20), 2948−2951.
(28) Yang, L.; Cheng, D.; Xu, H.; Zeng, X.; Wan, X.; Shui, J.; Xiang, Z.; Cao, D. Unveiling the high-activity origin of single-atom iron catalysts for oxygen reduction reaction. *Proc. Natl. Acad. Sci. U. S. A.* **2018**, *115* (26), 6626−6631.
(29) Liu, K.; Fu, J.; Lin, Y.; Luo, T.; Ni, G.; Li, H.; Lin, Z.; Liu, M. Insights into the activity of single-atom Fe-N-C catalysts for oxygen reduction reaction. *Nat. Commun.* **2022**, *13* (1), 2075.
(30) Hammer, B.; Hansen, L. B.; Nørskov, J. K. Improved adsorption energetics within density-functional theory using revised Perdew-Burke-Ernzerhof functionals. *Phys. Rev. B* **1999**, *59* (11), 7413−7421.
(31) Perdew, J. P.; Burke, K.; Ernzerhof, M. Generalized Gradient Approximation Made Simple. *Phys. Rev. Lett.* **1996**, *77* (18), 3865−3868.
(32) Blöchl, P. E. Projector augmented-wave method. *Phys. Rev. B* **1994**, *50* (24), 17953−17979.
(33) Kohn, W.; Sham, L. J. Self-Consistent Equations Including Exchange and Correlation Effects. *Phys. Rev.* **1965**, *140* (4A), A1133−A1138.
(34) Giannozzi, P.; Baroni, S.; Bonini, N.; Calandra, M.; Car, R.; Cavazzoni, C.; Ceresoli, D.; Chiarotti, G. L.; Cococcioni, M.; Dabo, I.; et al. QUANTUM ESPRESSO: a modular and open-source software project for quantum simulations of materials. *J. Phys.: Condens. Matter* **2009**, *21* (39), No. 395502.
(35) Kelly, S. R.; Kirk, C.; Chan, K.; Nørskov, J. K. Electric Field Effects in Oxygen Reduction Kinetics: Rationalizing pH Dependence at the Pt(111), Au(111), and Au(100) Electrodes. *J. Phys. Chem. C* **2020**, *124* (27), 14581−14591.
(36) Hansen, H. A.; Viswanathan, V.; Nørskov, J. K. Unifying Kinetic and Thermodynamic Analysis of 2 e− and 4 e− Reduction of Oxygen on Metal Surfaces. *J. Phys. Chem. C* **2014**, *118* (13), 6706−6718.
(37) Duan, Z.; Henkelman, G. Theoretical Resolution of the Exceptional Oxygen Reduction Activity of Au(100) in Alkaline Media. *ACS Catal.* **2019**, *9* (6), 5567−5573.
(38) Le, J. B.; Fan, Q. Y.; Li, J. Q.; Cheng, J. Molecular origin of negative component of Helmholtz capacitance at electrified Pt(111)/water interface. *Sci. Adv.* **2020**, *6* (41), No. eabb1219.
(39) Mathew, K.; Kolluru, V. S. C.; Mula, S.; Steinmann, S. N.; Hennig, R. G. Implicit self-consistent electrolyte model in plane-wave density-functional theory. *J. Chem. Phys.* **2019**, *151* (23), 234101.
(40) Gauthier, J. A.; Dickens, C. F.; Chen, L. D.; Doyle, A. D.; Nørskov, J. K. Solvation Effects for Oxygen Evolution Reaction Catalysis on IrO2(110). *J. Phys. Chem. C* **2017**, *121* (21), 11455−11463.
(41) Tripkovic, V.; Skúlason, E.; Siahrostami, S.; Nørskov, J. K.; Rossmeisl, J. The oxygen reduction reaction mechanism on Pt(111) from density functional theory calculations. *Electrochim. Acta* **2010**, *55*, 7975−7981.
(42) Liu, S.; White, M. G.; Liu, P. Mechanism of Oxygen Reduction Reaction on Pt(111) in Alkaline Solution: Importance of Chemisorbed Water on Surface. *J. Phys. Chem. C* **2016**, *120* (28), 15288−15298.

https://doi.org/10.1021/jacs.3c11246
J. Am. Chem. Soc. 2024, 146, 3210−3219